Micronodule Detection and False-Positive Elimination from 3D Chest CT

Sukmoon Chang

Computer Science, Capital College, Penn State Univ.,
Middletown, PA 17057, USA

ABSTRACT

Computed Tomography (CT) is generally accepted as the most sensitive way for lung cancer screening. Its high contrast resolution allows the detection of small nodules and, thus, lung cancer at a very early stage. In this paper, we propose a method for automating nodule detection from high-resolution 3D chest CT images. Our method focuses on the detection of both calcified (high-contrast) and noncalcified (low-contrast) granulomatous nodules less than 5mm in diameter, using a series of 3D filters including a filter for vessels and noise suppression, a filter for nodule enhancement, and a filter for false-positive elimination based on local skeletonization of suspicious nodule areas. We also present promising results of applying our method to various clinical chest CT datasets with over 90% detection rate.

Keywords: Computed Tomography, Granulomatous Nodules, Computer Asisted Nodule Detection, Filter-Based Nodule Detection, False-Positive Elimination, Skeletonization.

1. INTRODUCTION

Early detection of lung cancer is critical to improving chances of survival. The five-year survival rate of lung cancer patients can reach 85%, if it is diagnosed in an early stage and surgery is possible [1, 2]. Nevertheless, only 15% of lung cancer cases are found at the localized early stage. For early diagnosis of lung cancer, it is critical to detect nodules less than 5mm in diameter.

Chest radiographs are still widely used for lung cancer screening and various computational methods have been developed to automate nodule detection from chest radiographs [22]. However, the low sensitivity of radiographs to small nodules restricts current systems to the detection of nodules larger than 1cm in diameter. On the other hand, the use of Computed Tomography (CT) is now generally accepted as the most sensitive way for lung cancer screening. While still somewhat controversial, low-dose helical CT has been suggested as a lung cancer screening method,

particularly in high risk patients. With its high contrast resolution, CT makes it possible to detect nodules of small size as well as nodules of low-contrast that are hard to be seen on conventional radiographs [13].

In this paper, we describe a method for automating nodule detection and false-positive elimination from high-resolution chest CT images. Our method focuses on the detection of both calcified and noncalcified discrete types of granulomatous nodules less than 5mm in diameter, using a series of 3D filters. Since pulmonary nodules can be anywhere inside lung, we first describe a filter to suppress vessels and noise. Moreover, noting that many malignant nodules are noncalcified and of low-contrast, we describe a filter to further enhance nodule intensity values. Finally, we propose a new method for false-positive elimination based on local skeletonization around suspicious nodule areas. We also present promising results of applying our method to various clinical chest CT datasets.

2. BACKGROUND

Pulmonary nodule detection is one of the most challenging tasks in medical imaging. Various factors can hinder the automatic detection of nodules. Some factors are related to nodule properties, while others are related to the complex lung geometry. The appearance of discrete nodules in a lung can arise from many different etiologies. In addition to primary or metastatic malignancies, there may be benign nodules of various types in the lung. While calcified nodules are more likely to be benign than malignant, many benign nodules are not calcified. Moreover, malignant nodules may occasionally contain calcifications. Other morphologic features are similarly nonspecific in distinguishing benign from malignant nodules.

Most frequently used properties of nodules in automatic detection are the shape, size, and intensity profile. Template matching techniques such as Gaussian-based nodular models [15] and cylindrical vascular models along with spherical nodular models [21] have been used to explore these features. Various pattern

recognition techniques such as fuzzy clustering [12], a linear discriminant classifier [3, 14], rule-based classification [4], and patient-specific a priori model [5] have also been used.

A filtering technique called *Quoit filter* has shown promising results [23], although it fails when nodules do not match with the filter in size or when nodules are not sufficiently isolated from nearby or penetrating vessels. To remedy the deficiencies of the Quoit filter, Miwa et. al. developed the *Variable N-Quoit filter* [18]. However, their system for nodule detection using the new filter dramatically increased the number of false positives. In addition, their system is overly complicated involving two 2D Quoit filtering and a 3D Quoit filtering process.

We proposed earlier a 3D filter-based nodule detection system based on Quoit filter, which was more natural and intuitive 3D extension of Quoit filter [8]. The system was composed of three filters, including a filter for vessels and noise suppression, a filter for nodule enhancement (based on Quoit filter), and a filter for false-positive elimination. However, the filter for false-positive elimination used a rather heuristic evaluation and may result in false-negative classification.

This paper furthers our previous system and proposes a new and novel method for false-positive elimination based on local skeletonization. Our focus is on the automatic detection of granulomatous nodules from chest CT images. Although granulomatous nodules frequently have higher intensity values than surrounding regions due to extensive calcification, most malignant nodules are noncalcified and, thus, of lower contrast. Our system targets both calcified (high-constrast) and noncalcified (low-constrast) granulomatous nodules less than 5mm in diameter.

3. METHOD

We propose a novel and efficient method for automatic micronodule detection and false-positive elimination from 3D chest CT images. The proposed method is based on the system we developed earlier [8] and improves its accuracy in terms of sensitivity and specificity. Our primary focus is on the detection of both calcified and noncalcified discrete types of granulomatous nodules less than 5mm in diameter.

The challenging problem for any automatic nodule detection system is to keep low false-positive detection rate while maintaining high sensitivity. Our earlier system proposed a series of 3D filters for automatic micronodule detection from chest CT images. As with most automatic nodule detection systems, our system initially detects many false-positive nodules. To eliminate false-positive nodules, we introduced another
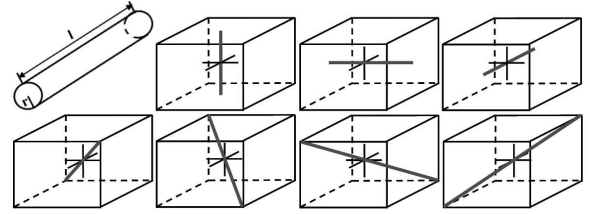

Figure 1: Cylinder filter and its orientations.

filter based on rather heuristic criteria and pointed out the need for a better method for false-positive elimination. This paper furthers the development of our earlier system and focuses on the false-positive elimination.

In this section, we first describe a series of 3D filters for automatic micronodule detection from chest CT images developed in our earlier system. Then, we point out a difficulty with the filter for false-positive elimination. Finally, we propose a new and improved method for false-positive elimination, based on the local skeletonization of the area surrounding each candidate nodule.

Micronodule Detection

Our approach for micronodule detection is composed of three steps: 1) vessels and noise suppression, 2) nodule enhancement, and 3) false-positive elimination.

Vessels and Noise Suppression: The primary task of the proposed system is to detect micronodules from 3D chest CT images in the presence of a background of many vessels and noise. The task may be made more difficult when nodules are adjacent to vessels, fissures, or lung wall. To address this difficulty, we first apply a cylinder filter to suppress intensity values of vessels and other elongated structures inside the lung, while maintaining nodule intensity values intact. The cylinder filter is defined as:

$$F_{\text{cyl}}(\vec{x}) = \max_{\theta} \left(\min_{\vec{y} \in \Omega_{\theta}^{\vec{x}}} I(\vec{y}) \right) \qquad (1)$$

where, I is the 3D image function and $\Omega_{\theta}^{\vec{x}}$ the domain of a cylinder centered at $\vec{x}$ with orientation θ. F_{cyl} is a hybrid maxmin neighborhood filter that produces strong responses to cylindrical enlongated regions (i.e., vessels). In this paper, we have selected the parameters of F_{cyl} empirically and used a cylinder with radius of 2 voxels and length of 7 voxels at 7 different orientations, as shown in Fig 1.

To suppress vessel intensity with F_{cyl}, we use

$$I'(\vec{x}) = I(\vec{x}) - F_{\text{cyl}}(\vec{x}) \qquad (2)$$

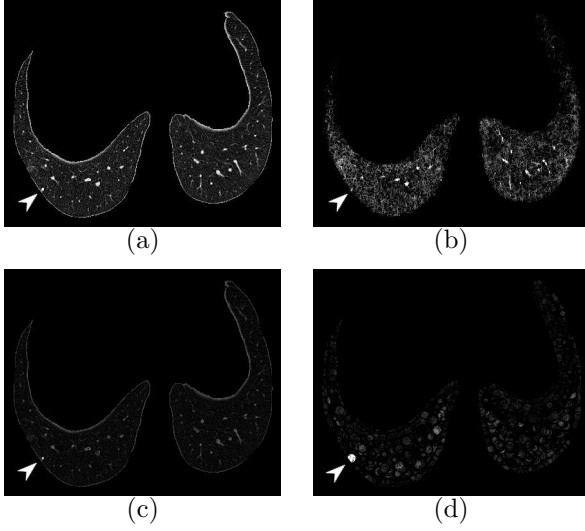(a)   (b)

(c)   (d)

Figure 2: Filtered images. (a) Original image I, (b) Image filtered with F_{cyl}, (c) Image filtered with $I - F_{\mathrm{cyl}}$, and (d) Final image filtered with F_{sph}. The arrow in each image points to the location of a nodule.

Applying F_{cyl} as in Eq. (2), the vessel intensity values are effectively suppreseed while the nodule intensity values remain almost intact. Fig. 2(b) illustrates the result of applying F_{cyl} to a dataset containing the original images in (a). It can be easily seen from the figure that F_{cyl} responded strongly to vessels but weakly to the nodule. By subtracting the two images in Fig. 2(a) and (b) using Eq. (2), we obtain a new image shown in Fig. 2(c). In the figure, we can see that vessels and noise are effectively suppressed while the nodule intensity remains intact.

Nodule Enhancement: Feature-based approaches for pulmonary nodule detection have shown promising results. The features most widely used are the size, shape, and intensity of nodules [3, 4, 23]. Granular nodules tend to be spherical with higher intensity than surrounding regions. However, many malignant nodules are noncalcified and of relatively low contrast. In order not to miss noncalcified low-contrast nodules, we enhance the intensity values of nodule areas (i.e., spherical regions with relatively high intensity compared to surrounding regions) by applying a non-linear sphere filter.

The response of the sphere filter F_{sph} at a point $\vec{x}$ is defined as:

$$F_{\mathrm{sph}}(\vec{x}) = \max_{\vec{y} \in S_r(\vec{x})} I'(\vec{y}) \quad - \max_{\vec{y} \in S_r(\vec{x}) - S_{r'}(\vec{x})} I'(\vec{y}) \quad (3)$$

where, $r > r'$ and $S_r(\vec{x})$ is the domain of a sphere of radius r centered at $\vec{x}$ (see Fig. 3). F_{sph} responds strongly to isolated spherical nodules and weakly to cylindrical vessels. Note that F_{sph} fails to produce
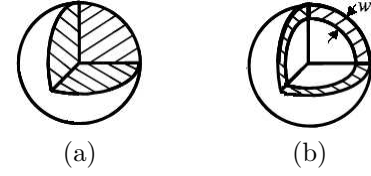

(a)   (b)

Figure 3: Domains of the sphere filter (Shaded regions). (a) S_r and (b) $S_r - S_{r'}, r > r'$.

strong responses to nodules when the size of a nodule does not match with the size of F_{sph}. In other words, the size of nodules to be detected is determined by the size of F_{sph}. In order to detect variable sizes of nodules, we follow the approach in [18] and employ the adaptive F_{sph} whose size is optimally adjusted by

$$r(\vec{x}) = r'(\vec{x}) + w \quad \text{and} \quad r'(\vec{x}) = \min_{\pi \in \Pi(\vec{x})} (|\pi|) \quad (4)$$

where, $\Pi(\vec{x})$ is the set of all paths from $\vec{x}$ to the background, $|\pi|$ is the length of a path π, and w is the width of the filter. The result of F_{sph} applied to a cylinder-filtered image is shown in Fig. 2(d). As expected, only the nodule produced strong response to F_{sph}. The large differences of the filter responses between nodules and vessel areas allow the automatic detection of pulmonary micronodules by a simple thresholding operation.

False Positive Elimination: The challenging problem for any automatic nodule detection system is to keep the false-positive detection rate low, while maintaining high sensitivity. In [8], we introduced a filter for sphericity test for false-positive elimination as follows. Let C be a cube surrounding a suspicious nodule area. The intensity values inside C are projected onto C along x, y, and z-axes by applying MIP [20], generating three 2D images, M_i, $i = 1, 2, 3$. The suspicious nodule area in each of these images is extracted separately by thresholding. To maintain the degree of automation, the three threshold values are automatically computed using a threshold selection method such as [19]. The sphericity test is then applied to the three segmented nodule areas. Let A_i and L_i be the area and the border length of the segmented nodules in M_i, respectively. Then, the sphericity of the segmented nodule area is measured using

$$F_{\mathrm{e}}^i = \frac{4\pi A_i}{L_i^2} \quad (5)$$

The final classification of a suspicious nodule was determined based on the fact that F_{e}^i is 1 for a circle and the more elongated the segmented nodule area, the weaker the response of F_{e}^i. The suspicious nodules were thus classified as false-positives and eliminated if
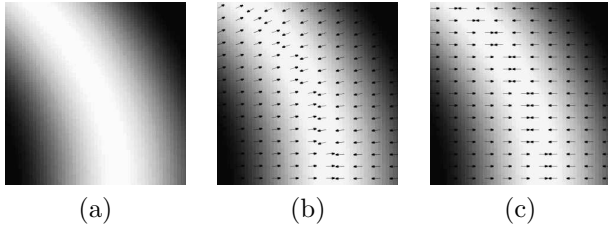
Figure 4: Sign barriers. (a) Curvilinear object, (b) Normalized gradient vectors, and (c) Normalized gradient vectors projected onto horizontal lines.

any of the three segmented nodule areas fails to pass the test.

This approach is rather heuristic, however, in that F_e^i assumes that the segmented nodule areas have smooth boundaries, which is rare in reality. It is easy to see that a segmented nodule with jagged boundary will fail the test. In the next section, we propose a new and novel method for false-positive elimination, based on local skeletonization of surrounding areas of suspicious nodules.

False-Positive Elimination with Local Skeletonization

The purpose of F_e^i was to test whether the segmented region of a suspicious nodule is elongated in shape (i.e., vessel) in any of the three directions, assuming that the segmented region has smooth boundary. As pointed out previously, however, a segmented nodule with jagged boundary will fail the test, resulting in a false-negative classification. In order to avoid the assumption and, thus, false-negative classification, we propose a novel method that directly measures the elongatedness of the segmented region of a suspicious nodule using local skeletonization method based on intensity ridges we developed earlier [7]. In grayscale images, including medical images, the objects of interest are usually identified as relatively brighter (or darker) regions and intensity ridges tend to be at the center of such regions at a given scale. Thus, intensity ridges have been used as a reliable approximation to the skeletons [9, 10, 11]. Without loss of generality, we assume that the objects of interest are brighter than the background and their centerlines coincide with the height ridge on the intensity profile.

It is well known that the gradient at any point on such objects generally points towards the ridge and reverses its direction as it crosses the ridge [6, 7, 16, 17]. Similarly, for a point to be on a ridge, it must be a local maximum on some direction, i.e., on a line passing through the point. Consider a line (L_θ) with an arbitrary orientation θ and three contiguous points (p_{-1}, p_0, p_{+1}) on it. If p_0 is on a ridge, the gradients at p_{-1} and p_{+1} must point toward

p_0, forming a sign barrier between them. Fig. 4 (b) illustrates an example of sign barriers around the ridge of a curvilinear structure in (a). Note that the sign barriers are not easily identifiable at some part of the object. We can enhance the sign barriers by projecting gradient vectors onto L_θ, as illustrated in (c), where $\theta = 0$ (horizontal lines) is used. In summary, if a ridge intersects L_θ, it generates a sign barrier on the line, i.e., between the two adjacent points that enclose the point of intersection.

It has been shown in [6, 7] that examining sign barriers on two projection lines, L_θ and $L_{\theta'}$, with sufficiently different orientations detects all the ridge points, leading to a simple scan-conversion algorithm for ridge point detection. Given a gradient vector field $\nabla I(x, y) = \langle v_x, v_y \rangle$, two vector fields ($N_\theta$ and $N_{\theta'}$) are computed by projecting the gradients onto L_θ and $L_{\theta'}$, respectively. For L_θ and $L_{\theta'}$ to have sufficiently different orientations, we naturally use $\theta = 0$ and $\theta = 90$, and the projection simply becomes:

$$
\begin{aligned}
N_0(x, y) &= \langle \, \text{sign}(v_x), 0 \, \rangle \\
N_{90}(x, y) &= \langle \, 0, \text{sign}(v_y) \, \rangle \; .
\end{aligned}
$$

Then, the algorithm scans N_0 with L_0 from top to bottom and N_{90} with L_{90} from left to right. For each scan, it searches for sign barriers on L_0 from left to right and L_{90} from top to bottom. Finally, it combines the points of sign barriers on L_0 and L_{90}.

The scan-conversion algorithm is applied to each M_i of the three MIP images of the surrounding area of a suspicious nodule and the length l_i of the skeleton branch is measured in pixels. If $l_i/r > \delta$, where r is the radius of F_{sph} used to detect the candidate nodule (see Eq. (4)) and δ is a given constant, the nodule is classified as false positives. In this paper, we have empirically selected and used $\delta = 2r$.

4. RESULTS

We applied the method to clinical chest CT datasets containing 49 nodules. The datasets were digitally resliced to ensure cubic voxels and the lung areas were extracted. The vessels and noise in the lung areas were first suppressed using the cylinder filter. We have selected the parameters of the filter empirically and used a cylinder with radius of 2 voxels and length of 7 voxels at 7 orientations. The results were filtered again with the sphere filter to enhance nodule intensities. Then, suspicious nodule regions were extracted and skeletonized using scan-conversion algorithm for false-positive elimination. Our method reported 52 nodules and an experienced radiologist verified that all the 49 nodules present in the datasets were correctly identified and confirmed that they were

Table 1: Results.

Radiologist's Reading	Before FP Elimination	After FP Elimination	TP	FP	FN
49	97	52	49	3	0

less than 5mm in diameter. The results are summarized in Table 1. Although our method detected all the 49 nodules present in the datasets without false-negative nodules, it also reported 2 false-positive nodules. These cases were cause by abrupt intensity changes in small regions of vessels, which are very similar to nodules penetrated by vessels. Fig. 5 shows typical cases of the detected nodules. In each pair of images in the figure, the processed image is shown on the left and the original image on the right. The method successfully detected nodules that are close to lung walls (Fig. 5 (a)), sufficiently isolated nodules (Fig. 5 (b)), nodules with nearby vessels (Fig. 5 (c)), nodules with penetrating vessels and nodules adjacent to a fissure (Fig. 5 (d,e,f)).

5. CONCLUSIONS

We have introduced a series of filters for automated micronodule detection from 3D chest CT. These include a cylinder filter for vessel and noise suppression, which generates sufficient gaps in intensities between nodule and vessel regions for further processing. Then, the sphere filter was introduced for nodule enhancement, which was a natural 3D extension of 2D Quoit filter. Finally, we proposed a method for false-positive elimination based on the local skeletonization of surrounding regions of suspicious nodules.

We conducted a preliminary set of experiments with our method on clinical chest CT datasets. The experiments confirmed that the proposed method was able to detect various nodules, including nodules with nearby vessels or even nodules with penetrating vessels and fissures. The datasets contained 49 nodules with diameter less than 5mm and the method detected all the nodules without false-negative classification. However, it also reported 3 false-positive cases. These cases result from the abrupt intensity changes on small regions of vessels, which is very hard to differentiate from nodules with penetrating vessels. With the promising preliminary results, we plan to further our experiments in the future to obtain statistically useful validation.

REFERENCES

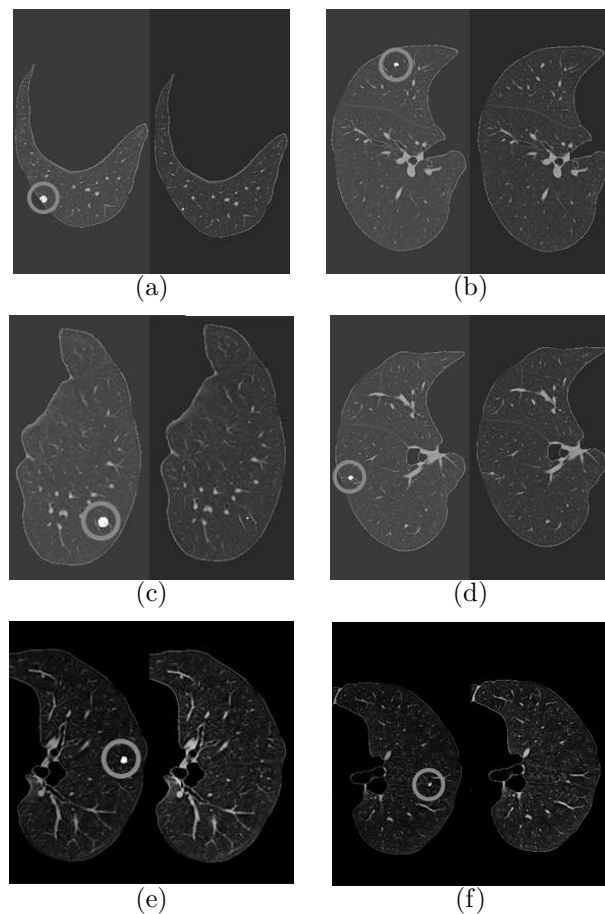[1] Alliance for Lung Cancer Advocacy, Support, and Education: Early Detection and Diagnostic Imaging (2001)

[2] American Cancer Society: Cancer Facts and Figures (2003)

[3] Armato, S.G., Giger, M.L., Moran, et. al.: Computerized Detection of Pulmonary Nodules on CT Scans. Radiographics **19** (1999) 1303–1311

[4] Betke, M., Ko, J.P.: Detection of Pulmonary Nodules on CT and Volumetric Assessment of Change over Time. MICCAI (1999) 245–252

[5] Brown, M.S., McNitt-Gray, M.F., Goldin, et. al.: Patient-Specific Models for Lung Nodule Detection and Surveillance in CT Images. IEEE Trans. Med. Imag. **20:12** (2001) 1242–1250

Figure 5: Detected nodules. In each image, the processed image is shown on the left and the original image on the right.

[6] Chang, S., Kulikowski, C.A., Dunn, S.M., Levy, S.: Biomedical Image Skeletonization: A Novel Method Applied to Fibrin Network Structures. MedInfo (2001)

[7] Chang, S., Metaxas, D., Axel, L.: Scan-Conversion Algorithm for Ridge Point Detection on Tubular Objects. MICCAI (2003) 158–165

[8] Chang, S., Emoto, H., Metaxas, D., Axel, L.: Pulmonary Micronodule Detection from 3D Chest CT. MICCAI (2004) 821–828

[9] Eberly, D., Gardner, R., Morse, B., Pizer, S., Scharlach, C.: Ridges for Image Analysis. J. Math. Imag. Vis. **4** (1994) 353–373

[10] Gauch, J.M., Pizer, S.M.: The INtensity Axis of Symmetry and Its Application to Image Segmentation. PAMI **15:8** (1993) 753–770

[11] Haralick, R.M.: Ridges and Valleys on Digital Images. CVGIP **22** (1983) 28–38

[12] Kanazawa, K., Kawata, Y., Niki, N., et. al.: Computer-Aided Diagnosis for Pulmonary Nodules based on Helical CT Images. Comput. Med. Imag. Graph. **22:2** (1998) 157–167

[13] Kaneko, M., Eguchi, K., et. al.: Peripheral Lung Cancer: Screening and Detection with Low-Dose Spiral CT versus Radiography. Radiology **201** (1996) 798–802

[14] Kawata, Y., Niki, N., Ohmatsu, H., et. al: Computer-Aided Diagnosis of Pulmonary Nodules Using Three-Dimensional Thoracic CT Images. MICCAI (2001) 1393–1394

[15] Lee, Y., Hara, T., Fujita, H, Itoh, S., Ishigaki, T.: Automated Detection of Pulmonary Nodules in Helical CT Images Based on an Improved Template-Matching Technique. IEEE Trans. Med. Imag. **20:7** (2001) 595–604

[16] López, A.M., Lumbreras, F., Serrat, J.: Creaseness from Level Set Extrinsic Curvature. ECCV (1998) 156–169

[17] Maintz, J.B., van den Elsen, P.A., Viergever, M.A.: Evaluation of Ridge Seeking Operators for Multimodality Image Matching. PAMI, Vol. 18, no. 4 (1996) 353–365

[18] Miwa, T., Kako, J., et. al.: Automatic Detection of Lung Cancers in Chest CT Images by the Variable N-Quoit Filter. Syst. Comput. Jpn. **33:1** (2002) 53–63

[19] Otsu, N.: A Threshold Selection Method from Gray-Level Histograms. IEEE Trans. Syst. Man and Cybern. **9:1** (1979) 62–66

[20] Sato, Y., Shiraga, N., Nakajima, S., Tamura, S., Kikinis, R.: LMIP: Local Maximum Intensity Projection–A New Rendering Method for Vascular Visualization. J. Comput. Assist. Tomogr. **22:6** (1998) 912-917

[21] Takizawa, H., Shigemoto, K., Yamamoto, S.: A Recognition Method of Lung Nodule Shadows in X-Ray CT Images Using 3D Object Models. IJIG **3:4** (2003) 533–545

[22] van Ginneken, B., ter Haar Romeny, B.M., Viergever, M.A.: Computer-Aided Diagnosis in Chest Radiography: A Survey. IEEE Trans. Med. Imag. **20:12** (2001) 1228–1241

[23] Yamamoto, S., Matsumoto, M., Tateno, Y., et. al.: Quoit Filter: A New Filter Based on Mathematical Morphology to Extract the Isolated Shadow, and Its Application to Automatic Detection of Lung Cancer in X-ray CT. ICPR **2** (1996) 3–7